

Reflectance confocal microscopy of optical phantoms

Steven L. Jacques,^{1,*} Bo Wang,¹ and Ravikant Samatham¹

¹Department of Biomedical Engineering, Oregon Health & Science University, 3303 SW Bond Ave., Portland, OR 97239, USA

*jacquess@ohsu.edu

Abstract: A reflectance confocal scanning laser microscope (rCSLM) operating at 488-nm wavelength imaged three types of optical phantoms: (1) 100-nm-dia. polystyrene microspheres in gel at 2% volume fraction, (2) solid polyurethane phantoms (INO BiomimicTM), and (3) common reflectance standards (SpectralonTM). The noninvasive method measured the exponential decay of reflected signal as the focus (z_f) moved deeper into the material. The two experimental values, the attenuation coefficient μ and the pre-exponential factor ρ , were mapped into the material optical scattering properties, the scattering coefficient μ_s and the anisotropy of scattering g . Results show that μ_s varies as 58, 8–24, and 130–200 cm^{-1} for phantom types (1), (2) and (3), respectively. The g varies as 0.112, 0.53–0.67, and 0.003–0.26, respectively.

© 2012 Optical Society of America

OCIS codes: (290.0290) Scattering; (170.0170) Medical optics and biotechnology; (170.6935) Tissue characterization.

References and links

1. D. S. Gareau, Ph.D. thesis dissertation, "In vivo confocal microscopy in turbid media" (Oregon Health & Science University, 2006).
2. S. L. Jacques, D. Levitz, R. Samatham, D. S. Gareau, N. Choudhury, and F. Truffer, "Light scattering in confocal reflectance microscopy," in *Biomedical Applications of Light Scattering*, A. Wax and V. Backman, eds. (McGraw-Hill, 2010).
3. R. Samatham, S. L. Jacques, and P. Campagnola, "Optical properties of mutant versus wild-type mouse skin measured by reflectance-mode confocal scanning laser microscopy (rCSLM)," *J. Biomed. Opt.* **13**(4), 041309 (2008).
4. D. Levitz, M. T. Hinds, N. Choudhury, N. T. Tran, S. R. Hanson, and S. L. Jacques, "Quantitative characterization of developing collagen gels using optical coherence tomography," *J. Biomed. Opt.* **15**(2), 026019 (2010).
5. D. Levitz, M. T. Hinds, A. Ardeshiri, S. R. Hanson, and S. L. Jacques, "Non-destructive label-free monitoring of collagen gel remodeling using optical coherence tomography," *Biomaterials* **31**(32), 8210–8217 (2010).
6. R. Samatham, K. G. Phillips, and S. L. Jacques, "Assessment of optical clearing agents using reflectance-mode confocal scanning laser microscopy," *J. Innovative Opt. Health Sci.* **03**(03), 183–188 (2010).
7. S. L. Jacques, "The fractal nature of light scattering," *J. Innovative Opt. Health Sci.* **04**(01), 1–7 (2011).
8. R. A. McLaughlin, L. Scolaro, P. Robbins, C. Saunders, S. L. Jacques, and D. D. Sampson, "Parametric imaging of cancer with optical coherence tomography," *J. Biomed. Opt.* **15**(4), 046029 (2010).
9. L. Scolaro, R. A. McLaughlin, B. R. Klyen, B. A. Wood, P. D. Robbins, C. M. Saunders, S. L. Jacques, and D. D. Sampson, "Parametric imaging of the local attenuation coefficient in human axillary lymph nodes assessed using optical coherence tomography," *Biomed. Opt. Express* **3**(2), 366–379 (2012).
10. INO, Inc., "Biomimic—optical phantoms," (2012), <http://www.ino.ca/en-ca/achievements/description/project-optical-phantoms.html>.

1. Introduction

A variety of optical measurements can easily measure the absorption coefficient, μ_a [cm^{-1}], and the reduced scattering coefficient, $\mu_s' = \mu_s(1-g)$ [cm^{-1}], of a tissue sample. However, separation of μ_s' into the two factors, the scattering coefficient, μ_s [cm^{-1}], and the anisotropy of scattering, g [dimensionless], usually involves bench-top experiments with thin tissue slices. This paper describes a method that measures μ_s and g noninvasively on an intact tissue, which

is therefore useful for *in vivo* measurements of tissue optical properties [1]. This paper demonstrates the technique on some phantom tissues.

The method uses reflectance confocal scanning laser microscope (rCSLM), or alternatively optical coherence tomography (OCT), to scan into a sample material and observe the exponential decay of reflected signal as the focus is translated deeper into the sample. At deeper depths it is more difficult for photons to penetrate to the focus and scatter back out into the collection solid angle of the objective lens. Others have recognized that attenuation of an rCSLM or OCT signal could characterize tissues (see [2] for review). The key improvement of this proposed method is to incorporate scattering anisotropy into the treatment so as to separately specify μ_s and g .

The method has been used to study the scattering consequences of a single gene mutation in mouse skin [3], the scattering changes as cells remodel a collagen gel [4,5], and the scattering changes in mouse skin when soaked in glycerin to achieve optical clearing [6]. In all cases, the distinction between μ_s and g could be discerned. The g value is of particular interest since it relates to the size of scatterers [7]. The method has been used for enhanced image contrast in optical coherence tomography imaging of breast cancer lymph nodes [8,9].

The three types of phantoms tested were (1) polystyrene microspheres in a gel, (2) solid polyurethane phantoms, and (3) a well-known commercial reflectance standard.

The goal of this report is to illustrate the use of the rCSLM technique as applied to solid phantoms and to offer an initial characterization of the μ_s and g of the phantoms.

2. Methods

2.1. Phantoms

A set of five phantom materials were tested:

1. Polystyrene microspheres in aqueous agarose gel.

The sphere diameter was 100-nm at a volume fraction of 2%. The refractive indices at 488 nm were $n_{\text{spheres}} = 1.599$ for spheres and $n_{\text{water}} = 1.336$ for the aqueous gel (98% water). The gel was held between a 1-mm-thick glass slide and a 120- μm -thick coverslip. One location on phantom was tested, since such gels are routinely measured in our lab.

2. Hard polyurethane phantom.

The phantom was obtained from INO, Inc., Canada, and is called Hard Biomimic phantom [9]. See Fig. 1(a). Three locations of the phantom were tested, but the results were very consistent for each site.

3. Soft polyurethane phantom.

The phantom was obtained from INO, Inc., Canada, and is called Soft Biomimic phantom. See Fig. 1(b). Again, three locations were tested.

4. SpectralonTM, 99% reflectance standard.

The reflectance standard was obtained from LabSphere, Inc. (New Hampshire, USA), and is now available from Pro-Lite Technology, Inc. See Fig. 1(c). One location tested.

5. SpectralonTM, 75% reflectance standard.

The reflectance standard was obtained from LabSphere, Inc. (New Hampshire, USA), and is now available from Pro-Lite Technology, Inc. See Fig. 1(c). One location tested.

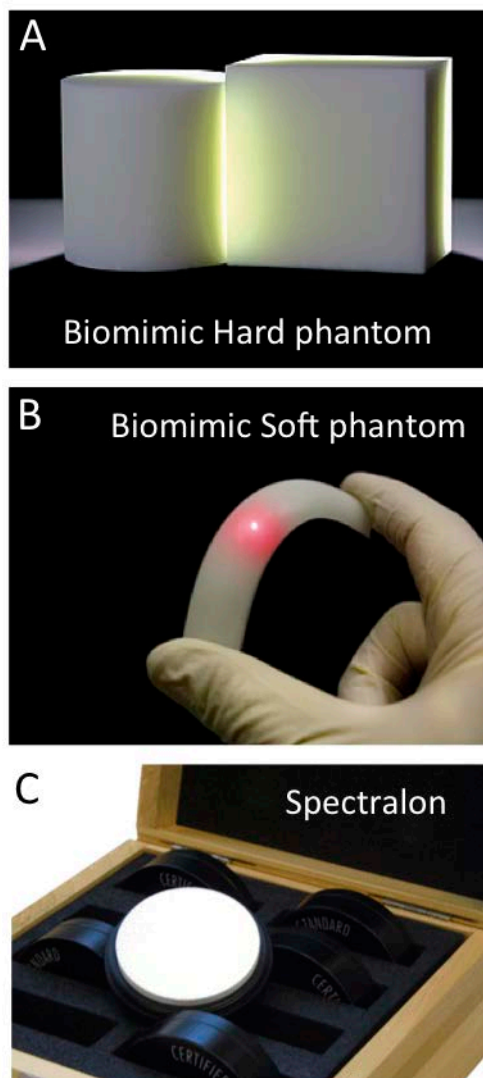


Fig. 1. The phantoms. (A) Hard Biomimic™ polyurethane phantom, INO, Inc., Canada. (B) Soft Biomimic™ polyurethane phantom, INO. (C) Spectralon™, Pro-Lite Technology, Inc. Not shown is the gel phantom composed of 1% volume fraction 100-nm-dia. polystyrene microspheres in aqueous agarose gel. (Photos A,B from Ref. 10.)

2.2. Confocal reflectance microscope

The confocal reflectance scanning laser microscope (rCSLM), built in our laboratory as an inverted microscope, has been used in previous studies [1–3,5,6]. An argon-ion laser delivered ~10 mW of 488-nm wavelength to the microscope objective lens. The objective lens (NA = 0.90, water-dripping lens, LUMPlanFL, Olympus America, Melville, New York) was water-coupled to the phantoms. For the microsphere gel, the microscope was water-coupled to the coverslip. Figure 2 shows the basic design. Lateral scanning was implemented by *x*- and *y*-galvo scanning mirrors (RS-15, Nutfield Technology Inc., Windham, New Hampshire), yielding 512 x 526 pixels of equal 0.312 μm size. Axial *z*-axis translation of the focus was achieved by translating the sample using a motorized scanning stage (LS50A, Applied Scientific Instrumentation, Eugene, Oregon), yielding 1- μm axial stepsizes in the axial region

of interest. However, to achieve a broader axial range of imaging, the axial stepsizes were increased to 5 or 10 μm at positions above and below this central region of 1- μm stepsizes. The detection arm was a lens/pinhole/photomultiplier-tube assembly (PMT: 5773-01, Hamamatsu Photonics, Japan). Scanning and detection were controlled by a data acquisition board (6062E, National Instruments, Austin, TX) and custom software developed using LabviewTM. Image reconstruction and analysis were done using MATLAB (Mathworks Inc., Natick, Massachusetts).

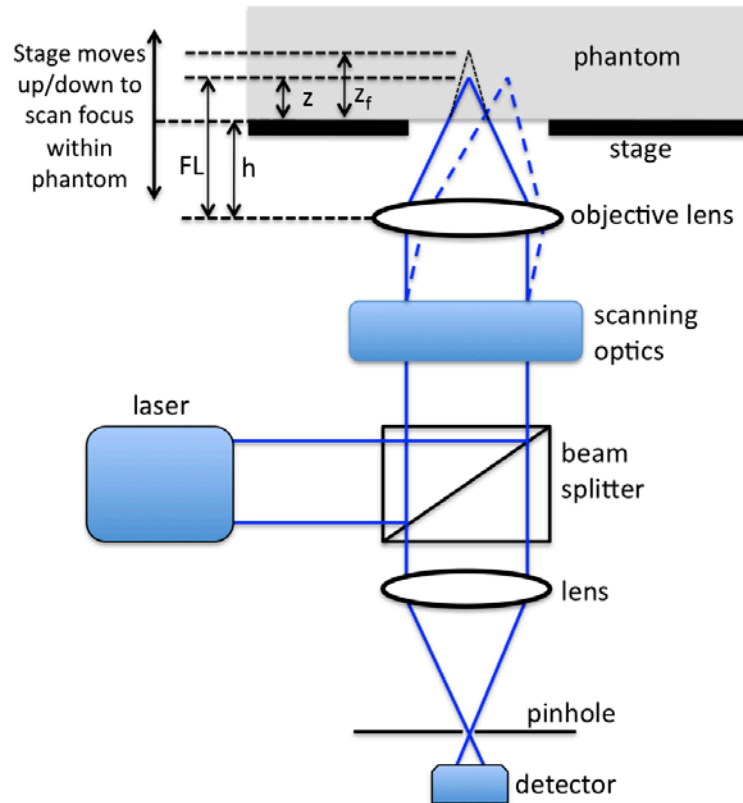


Fig. 2. Schematic of the reflectance confocal scanning laser microscope (rCSLM). Laser light is delivered to a focal volume within the phantom, and reflectance from this focus is returned through a pinhole to a detector. The sample stage moves the phantom up and down in order to scan the focus within the phantom.

2.3. Raw data acquisition

Figure 3 shows examples of the raw images of reflectance for the phantoms, shown as $\log_{10}(V(z,x))$ where V is the detector voltage. The abscissa, x , is the lateral position of the phantom. The ordinate, z , is the apparent depth of the focal volume equal to the difference between the focal length (FL) and the distance (h) between the objective lens and the phantom surface.

2.4. Calibration

Figure 4 shows the calibration of the system. The glass-water(gel) interface of the microsphere-water(gel) phantom was imaged to yield a peak voltage $V_{gw} = 5.14$ V. The expected reflectance from this interface was $r_{gw} = ((n_{\text{water}} - n_{\text{glass}}) / (n_{\text{water}} + n_{\text{glass}}))^2 = 0.00427$, where $n_{\text{glass}} = 1.522$. Then a calibration factor was calculated: $calib = r_{gw} / V_{gw} = 1.204 \times 10^{-4}$ [1/V]. Thereafter, any measurement V was multiplied by $calib$ to yield the reflectance R ,

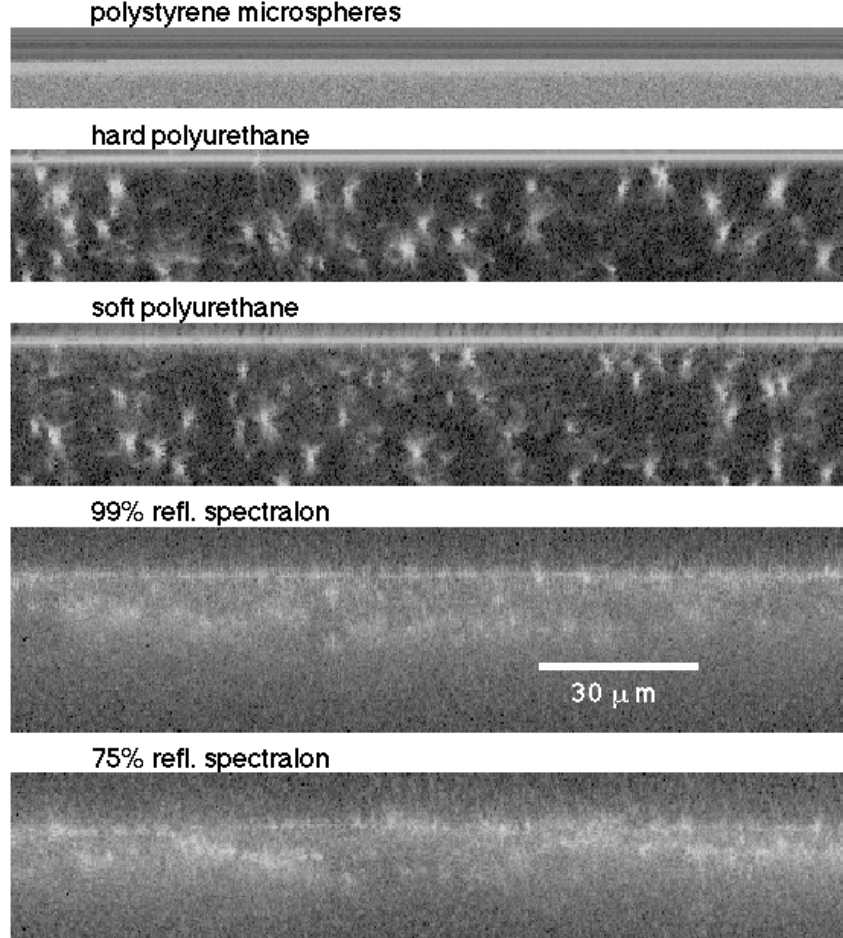


Fig. 3. Side-view confocal reflectance image in volts, $\text{image}(z,x)$ at $y = \text{middle of 3D image}$. The images show $\log_{10}(\text{voltage})$, where voltage encodes the reflectance. The color code is black = 0.01 V and white = 10 V. The axial stepsize, Δz , was 1 μm . The microspheres have a glass/gel interface, while others have a water/phantom interface.

which is the fraction of light delivered by the microscope that is returned into the microscope for detection.

To check the calibration, the axial profile, $R(z_f)$, for the polystyrene microsphere gel phantom was analyzed to fit the expression

$$R(z_f) = \rho e^{-\mu z_f} \quad (1)$$

As the distance height (h) of the lens above the surface of the phantom was changed, the apparent depth position of the focus varied as $z = \text{FL} - h$, where FL is the focal length of the lens. When $h = \text{FL}$, the focus is at the phantom surface. As h was decreased, z moved into the tissue. However the true position of the focus, z_f , increased as

$$z_f = \frac{\partial z_f}{\partial z} (z - D_{\text{glass}}) \quad (2)$$

where D_{glass} is the thickness of the glass coverslip if in place (if no glass, $D_{\text{glass}} = 0$). The parameter $\partial z_f / \partial z = \tan(\theta_1) / \tan(\theta_2)$, where $\theta_1 = \arcsin(\text{NA} / n_{\text{water}})$ and $\theta_2 = \arcsin(\text{NA} / n_{\text{phantom}})$. The factor $\text{NA} / n_{\text{phantom}}$ is referred to here as the *effective numerical aperture*. For the aqueous gel,

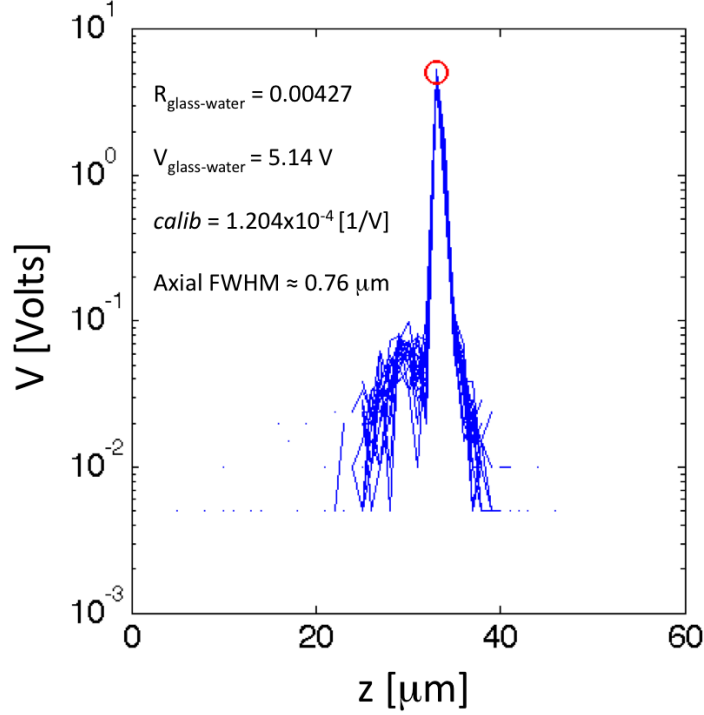


Fig. 4. Calibration of confocal reflectance measurement at 488 nm wavelength, using glass-water(gel) interface. Subsequent measurements of phantom are multiplied by *calib* ($1.204 \times 10^{-4} \text{ V}^{-1}$) such that a measurement of a glass-water interface will yield $R_{\text{glass-water}} = 0.00427$ and measurement of a mirror will yield $R_{\text{glass-water}} = 1$.

the value of $\partial z_f / \partial z$ was 1.00. For the polyurethane and SpectralonTM phantoms, the value of $\partial z_f / \partial z$ was 1.20, based on an assumed value of 1.49 for n_{phantom} . Hence, the original data versus z was converted to data versus z_f before subsequent analysis.

2.5. Analysis

The behavior of $R(z_f)$ depends on the parameters ρ and μ , which are described as

$$\mu = (\mu_s a(g) + \mu_a) 2G \quad (3)$$

$$\rho = \mu_s \Delta z b(g) \quad (4)$$

where Δz is the standard axial resolution, $\Delta z = 1.4\lambda / \text{NA}^2$, where $\text{NA} = \sin(\theta_{1/2}) n_{\text{phantom}}$ with $\theta_{1/2}$ equal to the half angle of light delivery within the phantom and n_{phantom} is the refractive index of the phantom [2,3]. The value of n_{phantom} for the polyurethane and SpectralonTM phantoms was assumed to be 1.49.

In Eq. (2), μ refers to the attenuation of light as photons move to/from the focus. When scattering is very forward directed, it is possible for photons to still reach the focus despite multiple scattering. The function $a(g)$ varies from 1 to 0 as g varies from 0 to 1, i.e., from isotropic scattering to forward-directed scattering. The function was determined by Monte Carlo simulations of focused light penetration to a focus at z_f for varying values of μ_s at a given g . The change in fluence rate at the focus versus value of μ_s , or $F(\mu_s)$ at constant g , was fit by Eqs. (1)–(3) to specify the value of a . Repeating for different values of g yielded the function $a(g)$, which can be described as [2,3]

$$a(g) = 1 - \exp\left(-\frac{(1-g)^{0.6651}}{0.1555}\right). \quad (5)$$

The effect of absorption, μ_a , is negligible unless working with a very strongly absorbing material. The factor 2 accounts for the round-trip in/out path of collected photons. The factor G is a geometry factor that accounts for the extra pathlength of photons when a high NA objective lens is used. The value of G depends on the NA of the lens, and is approximated by

$$G = \left\langle \frac{1}{\cos(\theta)} \right\rangle = \frac{\int_{\pi-\theta_2}^{\pi-\theta_2} \frac{E_{\text{Gaussian}}(\theta)T(\theta)}{\cos(\theta)} 2\pi \sin(\theta) d\theta}{\int_{\pi}^{\pi-\theta_2} E_{\text{Gaussian}}(\theta)T(\theta) 2\pi \sin(\theta) d\theta} \quad (6)$$

where value θ_2 is the maximum half-angle of collection at the phantom surface, which depends on the NA of the lens. The factor $E_{\text{Gaussian}}(\theta) = \exp(-(\theta/\theta_2)^2)$ is a Gaussian function that describes the angular dependence of light entering the phantom. The assumption here is that the $\pm 1/e$ portion of the laser beam was filling the back pupil of the objective lens and reaching the phantom. This assumption is easily modified in Eq. (6) to match a particular experimental setup. The factor $T(\theta)$ is the transport to the focus from a surface entry point at an angle θ with respect to the central z axis. Attenuation of $T(\theta)$ by tissue scattering and absorption decreases the contribution from light at larger angles of entry, which slightly decreases the average pathlength, Gz_f , of photons reaching the focus. Equation (6) is more fully discussed in [2]. In this experiment, $G = 1.132$.

The function $b(g)$ describes the fraction of photons scattered within the axial Δz extent of the focus which are scattered back into the solid angle of collection of the objective lens. The function $b(g)$ is approximated by the integral over all angles of backscatter that are within the collection angle of the objective lens:

$$b(g) = \int_{\pi}^{\pi-\theta_2} p(\theta) 2\pi \sin(\theta) d\theta \quad (7)$$

where the scattering function $p(\theta)$ indicates the deflection of photons from their incident forward direction, π is the direct backscatter angle in radians and θ_2 is the maximum half-angle of collection by the lens in radians. The function $p(\theta)$ was approximated by the Henyey-Greenstein function:

$$p(\theta) = \frac{1}{4\pi} \frac{(1-g)^2}{(1+g^2-2g\cos(\theta))^{3/2}} \quad (8)$$

For the conditions of this experiment, $b(g) \approx 0.203\exp(-1.716g) - 0.077\exp(-0.744g)$, which equals 0.132 at $g = 0$, drops by 50% at $g = 0.262$ and drops by 90% at $g = 0.732$. Using Mie theory to generate $p(\theta)$ yields a similar $b(g)$ as the Henyey-Greenstein function, except when the spheres are large and scattering is very forward directed (not shown).

The effective solid angle of collection by the objective lens was also dependent on the refractive index of the phantom. The θ_2 is the maximum angle of collection by the lens, and was used in the calculation of $b(g)$ in Eq. (3).

The functions $a(g)$, $b(g)$ and $G(NA, g)$ continue to be topics of ongoing investigation.

Figure 5 shows an example analysis. A superficial region (5-50 μm below the surface) was used for fitting, beyond the effects of the front surface reflectance and before diffuse light begins to contaminate the signal. The noise floor due to diffuse light reflectance escaping within the solid angle eventually collected by the detector pinhole becomes important when the focus is located at depths beyond the transport mean free path, $1/(\mu_s(1-g))$. Hence, useful measurements are restricted to the superficial layer.

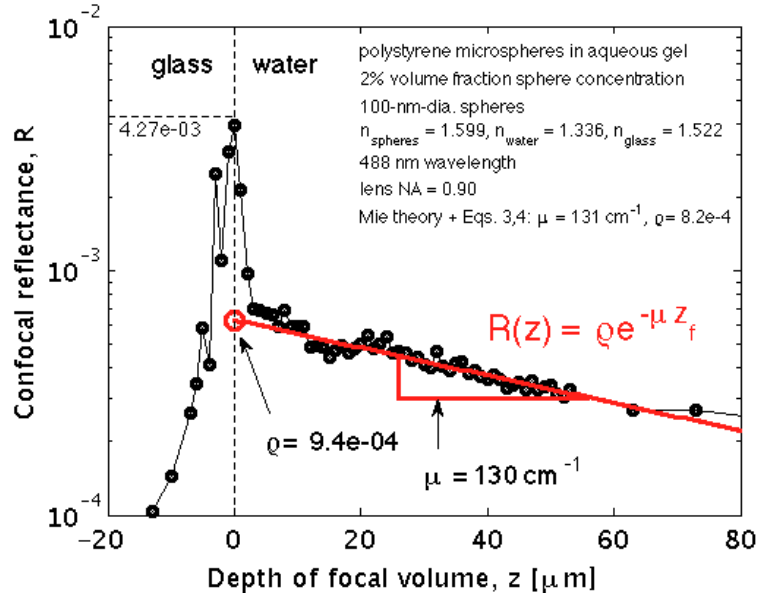


Fig. 5. Axial profile of confocal reflectance versus depth of focus, $R(z_f)$. The reflectance from the glass-gel interface was assumed to match the specular reflectance of a glass-water interface, $R_{\text{glass-water}} = 0.00427$, and was used to scale the laboratory counts. Hence, $R(z_f)$ is calibrated such that reflectance from a mirror in the focus yields $R = 1$. The exponential red line is $R(z_f) = \rho \exp(-\mu z_f)$. The value ρ is the extrapolated red line value at $z_f = 0$. The value μ is specified by the slope.

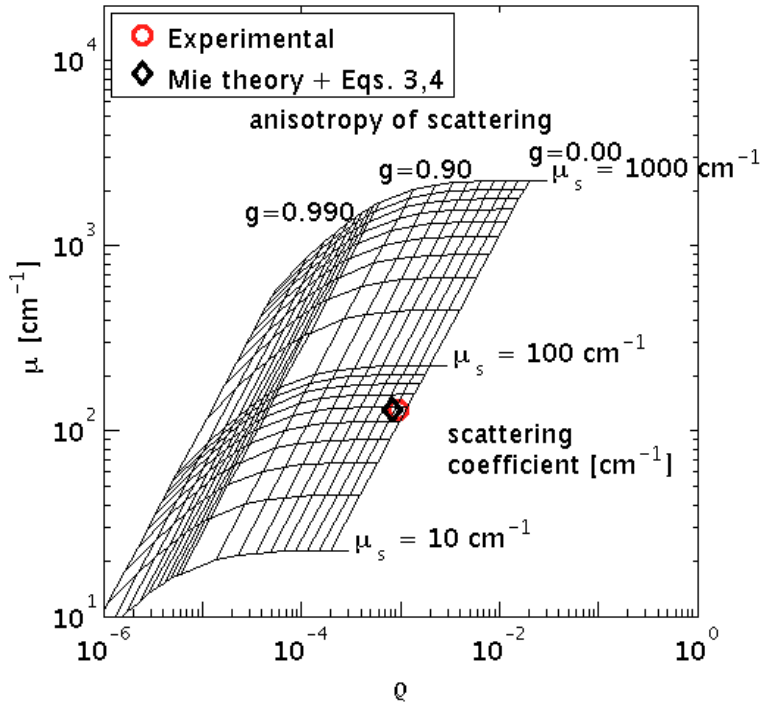


Fig. 6. Calibration grid with experimental data (red circle) and the Mie theory prediction (black diamond) using Eqs. (3), (4) for the polystyrene microsphere gel of Fig. 5. Mie theory predicts $\mu_s = 58.2 \text{ cm}^{-1}$, $g = 0.129$, and Eqs. (3), (4) predict $\mu_{\text{MIE}} = 131 \text{ cm}^{-1}$, $\rho_{\text{MIE}} = 8.2 \times 10^{-4}$. The experiment presents $\mu = 130 \text{ cm}^{-1}$, $\rho = 9.2 \times 10^{-4}$, and $\mu_s = 57.7 \text{ cm}^{-1}$, $g = 0.072$.

Figure 6 plots the mean μ versus mean ρ from Fig. 5 on a log-log plot. Superimposed on this plot is a grid of iso- g lines and iso- μ_s lines, based on Eqs. (3) and (4). This grid allows interpretation of the μ and ρ data in terms of the optical properties μ_s and g . The experimental data point (red circle) indicates $\mu_s = 57.7 \text{ cm}^{-1}$, $g = 0.072$, $\mu = 130 \text{ cm}^{-1}$, $\rho = 9.2 \times 10^{-4}$. Also shown is the predicted data point using Mie theory (black diamond), which has values of $\mu_{s,MIE} = 58.2 \text{ cm}^{-1}$, $g_{MIE} = 0.129$, $\mu_{MIE} = 131 \text{ cm}^{-1}$, $\rho_{MIE} = 8.2 \times 10^{-4}$. Work continues on testing the accuracy of the first-order theory (Eqs. (3), (4)) and on experimental methods for preparing microsphere gels for calibration.

3. Results

The images of Fig. 3 show that the solid phantoms (polyurethane and SpectralonTM) presented a low density of TiO_2 particles that strongly scattered light. These phantoms did not present a uniform attenuation $R(z_f)$ within the range of imaging that could be reliably analyzed using Eqs. (1)–(3). Nevertheless, the data was fit by Eq. (1) to yield μ and ρ experimental values.

Figure 7 shows axial profiles of 15 random x, y positions in the phantoms. The curves indicate a slow attenuation of signal as the focus is moved deeper into the tissue. Red lines indicate a slow attenuation of signal as the focus is moved deeper into the tissue. Red lines

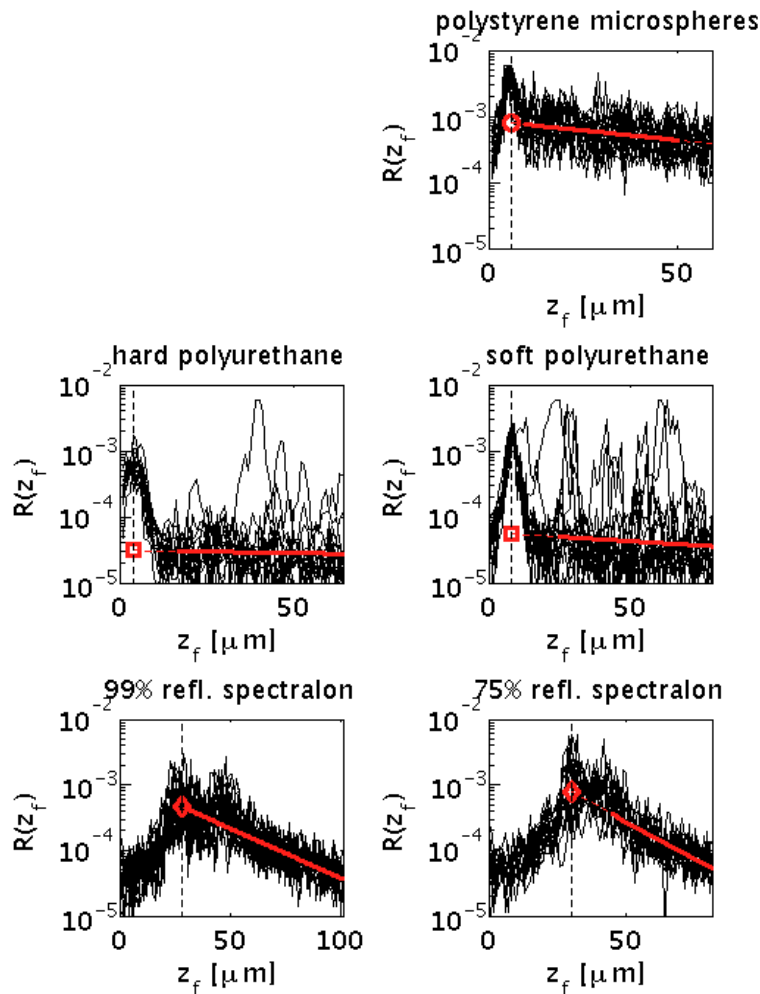


Fig. 7. Sampling of 15 axial profiles for the phantoms. The polyurethane phantoms have a baseline of low reflectance at the noise level of the measurement, but there are occasional spikes of reflectance from local strong reflectors. Bold red lines are exponential fits to the data, which is extrapolated to the front surface, indicated by red symbol.

indicate exponential fits to the attenuation of the $R(z_f)$ signal (bold lines indicate region of data fitted), and the slopes specify the values of μ . The fit is extrapolated (dashed lines) to the front surface of the phantom to specify the value of ρ (indicated by red symbol).

Figure 8 plots the μ and ρ values specified by the fits shown as red lines in Fig. 7, and superimposes a grid of iso- μ_s and iso- g lines to aid interpretation. The grid is drawn assuming the lens is water coupled to an aqueous gel ($n = 1.336$). There is agreement between the experimental measurement and Mie Theory for the microsphere gel. The grid slightly shifts downward when the lens is water coupled to the phantom polymer materials (n assumed to be ~ 1.49) (grid not shown since shift is very small; the grid's μ and ρ drop $\sim 3\%$, so data are properly deduced to be $\sim 3\%$ higher than values calculated with the water-coupled grid). The analysis considered this effect when computing the values summarized in Table 1.

Table 1: Summary of phantom measurements and properties

phantom	μ [cm^{-1}]	ρ	μ_s [cm^{-1}]	g
Mie theory for microspheres	131.2	8.1×10^{-4}	58.2	0.112
polystyrene microsphere gel	135.5	8.6×10^{-4}	60.1	0.122
hard polyurethane (Biomimic TM)	6.4	3.1×10^{-5}	7.6	0.531
soft polyurethane (Biomimic TM)	50.9	5.8×10^{-5}	24.4	0.674
99% refl. Spectralon TM	289	1.2×10^{-3}	132	0.262
75% refl. Spectralon TM	439	3.8×10^{-3}	200	0.003

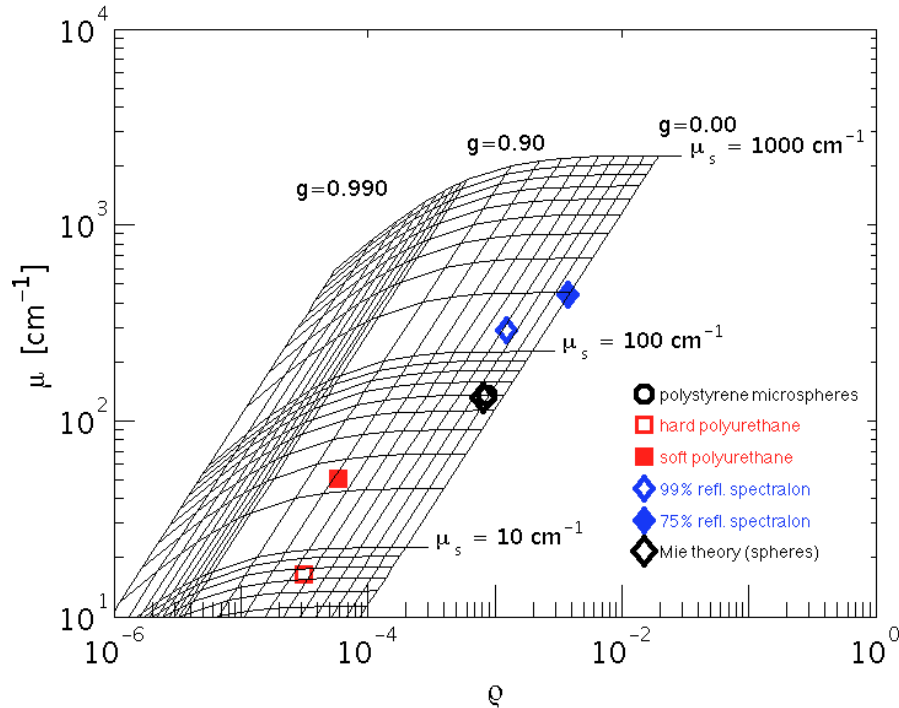


Fig. 8. Experimental attenuation vs reflectivity for phantoms at 488 nm wavelength, based on exponential fits of axial profiles (red lines in Fig. 7). The experimental measurement on polystyrene microspheres and the prediction of Mie theory are closely aligned.

4. Discussion

This pilot study of the optical properties of phantoms is intended to illustrate a noninvasive experimental approach toward specifying the optical scattering properties of a phantom, specifically the scattering coefficient (μ_s) and the anisotropy of scattering (g). The polyurethane phantoms (INO BiomimicTM) were shown to have a background optical properties along with a low density of dispersed strongly scattering TiO_2 particles. The

Spectralon™ phantoms were more dense in scattering, hence a higher μ_s than the polyurethane phantoms, and individual strongly scattering particles were present but less evident. The polystyrene microsphere gel phantom was the most uniform phantom, composed of a high concentration (2% volume fraction) of 100-nm-dia. spheres. Our experience with microsphere phantoms using larger spheres is that they also present as discrete strong scatterers. Therefore, we routinely use small 100-nm-dia. spheres when calibrating experiments.

Future work should explore the wavelength dependence of the μ_s and g values derived from axially scanned rCSLM signals. Comparison of the values against macroscopic measurements of the diffusion property $\mu_s' = \mu_s(1-g)$ should be made.

The method outlined in this paper can be used with any confocal microscope or OCT system operating in reflectance mode. The method has been used with a variety of systems, both custom built and commercial. The μ measurement is easily accomplished if the axial stepsize between successive x,y images is known. The ρ measurement requires calibration, however, such as the measurement of a glass/water interface, as in this paper. Alternatively, the measurement of a microsphere gel can be used to calibrate ρ . Since the anisotropy g is sensitive to ρ , the calibration is worthwhile if rCSLM or OCT is used to characterize the nanoarchitecture of a tissue.

Acknowledgments

We thank Jean-Pierre Bouchard from INO, Inc., Canada, for supplying the Hard Biomimic™ and Soft Biomimic™ phantoms. This work was funded in part by NIH R24-CA84587.